

Photometric Modulations on Intermediate Timescales in the Symbiotic Binaries

MELIS YARDIMCI* ¹, SAMET OK ¹ AND BELINDA KALOMENI ¹

¹*Department of Astronomy and Space Sciences, University of Ege, 35100, İzmir, Türkiye**

ABSTRACT

We present a multi-band study of three symbiotic binaries using combined ground- and space-based monitoring that spans up to 14 years. These datasets enable a systematic investigation of variability on intermediate timescales (tens of days) and the detection of shorter-period signals. All systems display coherent photometric modulations that are distinct from the orbital cycles. In AX Per, a dominant 75-day signal and its 37-day harmonic are identified, which we interpret as pulsations of the cool giant. CI Cyg exhibits a stable modulation between 70 and 74 days, which likely arises from a combination of pulsation and circumstellar or disk-related variability. For Z And, we confirm a persistent modulation between 55 and 60 days, consistent with semiregular pulsations of the cool component. Additionally, space-based data reveal further short-period variability, including coherent signals at 26.7 and 66.6 minutes in Z And and CI Cyg, respectively, and a quasi-periodic modulation near 0.95 days in AX Per. These detections suggest the presence of rapid activity driven by accretion or rotation, superposed on the intermediate timescale behavior. Our results show that the observed variability in these symbiotic binaries reflects the combined effects of cool giant pulsation, circumstellar or disk activity, and possible rotation of the hot component. The multi-timescale behavior revealed here offers new constraints on mass transfer and activity cycles in interacting binaries.

Keywords: Symbiotic binary stars (1674); Multi-color photometry (1077); Stellar Oscillation (1617); stars: individual (AX Per, CI Cyg, Z And)

1. INTRODUCTION

Symbiotic binaries (SySts) consist of an evolved red giant transferring mass to a compact hot companion, typically a white dwarf (K. Belczyński et al. 2000; U. Munari 2019; J. Merc 2025). Their light curves exhibit complex variability on multiple timescales: orbital modulations associated with eclipses and illumination effects (L. Formigini & E. M. Leibowitz 1990); long-term outbursts driven by changes in nuclear burning or accretion (J. Mikolajewska et al. 2002; J. L. Sokoloski et al. 2006b; A. R. King & J. E. Pringle 2009; D. A. Bollimpalli et al. 2018); and relatively short-term oscillations linked to pulsation, accretion instabilities (S. J. Kenyon 1986; J. Mikolajewska et al. 1995; U. Munari 2019), or possible white dwarf rotation (J. L. Sokoloski & L. Bildsten 1999; L. Formigini & E. M. Leibowitz 2009).

Despite decades of study, the intermediate regime between pulsational and orbital variability ($\approx 30\text{--}200$ d) remains poorly understood. Signals in this range have been reported sporadically in several systems (e.g., Z And, M. Sekeráš et al. 2019; A. Skopal et al. 2018), yet their physical origin and prevalence across symbiotic binaries have not been systematically investigated.

Photometric changes in symbiotic binaries arise from several interacting mechanisms that operate simultaneously. Orbital modulation produces eclipses or illumination effects as the red giant and ionized nebula move relative to the observer (L. Formigini & E. M. Leibowitz 1990; A. Skopal 2005). The cool giant often shows semiregular pulsations that generate variability on timescales of tens to hundreds of days (S. J. Kenyon 1986; L. Formigini & E. M. Leibowitz 1994; J. Mikolajewska et al. 2003). Mass-transfer fluctuations and instabilities in the accretion disk can introduce shorter-term variations, including flickering and quasi-periodic signals (J. L. Sokoloski & L. Bildsten 1999; G. J. M. Luna & J. L. Sokoloski 2007). During active phases, enhanced accretion or expansion of the hot component reshapes

¹ Released on ..., ...

* Corresponding author: melisyardimci@gmail.com;
melis.yardimci@mail.ege.edu.tr

the ionized nebula, producing complex multi-band light-curve behavior (A. Skopal 2003; J. L. Sokoloski et al. 2006b). These combined processes make the interpretation of photometric variability challenging and highlight the need for long-term, multi-band monitoring to separate orbital, pulsational, and accretion-driven components. The optical emission of symbiotic systems is a complex combination of radiation from three main components: the cool giant, the hot companion, and the surrounding ionized circumbinary nebula (U. Mürset et al. 1991; A. Skopal 2005). Consequently, separating the relative contributions of these components using photometric data alone is inherently difficult, particularly during active phases.

AX Per, CI Cyg, and Z And each exhibit additional system-specific properties that make them valuable laboratories for studying multi-timescale variability. AX Per is an eclipsing symbiotic binary with an orbital period of 682.1 ± 1.4 d (F. C. Fekel et al. 2000a), showing alternating quiescent and active phases in which its minima become distorted and asymmetric (L. Formigini & E. M. Leibowitz 1994; A. Skopal et al. 2001, 2011). CI Cyg, with an orbital period of 853.8 ± 2.9 d (F. C. Fekel et al. 2000a), hosts both a dense nebular region within the Roche lobe of the hot companion and a more extended bipolar structure (S. J. Kenyon et al. 1991), and its photometric behavior is strongly influenced by these components and by variable mass transfer (J. Mikolajewska et al. 2003; A. Skopal 2005). Z And, the prototype of symbiotic systems, has an orbital period of 759.0 ± 1.9 d (F. C. Fekel et al. 2000a) and undergoes recurrent optical outbursts (A. Skopal 2003). Its hot component shows rapid brightness modulations at 1682.6 ± 0.6 s (the quoted uncertainty reflects the formal statistical error; J. L. Sokoloski & L. Bildsten 1999) interpreted as the magnetic white dwarf’s spin period, making it a key system for investigating accretion-driven variability.

Outbursts in symbiotic binaries are commonly grouped into several categories. Z And-type outbursts exemplified by the recurrent activity of Z And itself, are characterized by a rapid rise in optical brightness followed by a slow decline that may persist for years or even decades (J. L. Sokoloski et al. 2006b; D. A. Bollimpalli et al. 2018). Early interpretations attributed Z And-type outbursts either to accretion-disk instabilities similar to those in dwarf novae (S. J. Kenyon 1986) or to the expansion and cooling of the hot component in response to enhanced accretion (J. Mikolajewska et al. 1995). More recent studies suggest that Z And-type outbursts result from a transient increase in the accretion rate that exceeds the level required to sustain sta-

Table 1. Observation log of AX Per, CI Cyg and Z And.

Name	Observatory	Filter/Sector	Starting	Ending
AX Per	T60	UBVR	May 2019	Oct 2024
	ASAS-SN	bc+bd	17 Dec 2014	20 Nov 2018
	KWS	BVIc	29 Aug 2011	8 Jan 2025
	S19	UBVRcIc	Nov 2011	Dec 2018
	TESS	Sector 58	29 Oct 2022	26 Nov 2022
CI Cyg	T60	UBVR	May 2019	Oct 2024
	ASAS-SN	bb	27 Mar 2015	23 Oct 2017
	KWS	BVIc	5 Jun 2011	29 Aug 2023
	S19	UBVRcIc	Nov 2011	Dec 2018
	TESS	Sector 74	03 Jan 2024	30 Jan 2024
	TESS	Sector 75	30 Jan 2024	26 Feb 2024
	TESS	Sector 81	15 Jul 2024	10 Aug 2024
	TESS	Sector 82	10 Aug 2024	05 Sep 2024
Z And	T60	UBVR	May 2019	Oct 2024
	ASAS-SN	ba	23 May 2015	26 Nov 2018
	KWS	BVIc	3 Aug 2011	28 Nov 2023
	S19	UBVRcIc	Nov 2011	Dec 2018
	TESS	Sector 57	30 Sep 2022	29 Oct 2022

ble burning on the white dwarf surface (e.g., A. Skopal et al. 2017; U. Munari 2019; A. Skopal et al. 2020). These results demonstrate that Z And-type outbursts can also occur in systems previously regarded as quiescent and underscore the importance of long-term photometric monitoring for constraining their physical origin. Symbiotic or slow novae evolve more gradually and are powered by thermonuclear flashes on the white dwarf surface (J. Mikolajewska et al. 2002; M. Kato & I. Hachisu 2023). Recurrent novae, such as RS Oph, occur in systems with massive white dwarfs that undergo repeated thermonuclear explosions on timescales of years to decades (J. L. Sokoloski et al. 2006a; G. J. M. Luna & J. L. Sokoloski 2007). These diverse outburst mechanisms illustrate the range of accretion and nuclear processes influencing the optical variability of symbiotic binaries and highlight the need to investigate how such activity couples to variability on intermediate and short timescales.

In this study, we perform a unified analysis of 14 yr of multiband ground-based photometry for AX Per, CI Cyg, and Z And, combined with complementary high-cadence observations from TESS. We aim to identify and compare intermediate-timescale modulations across the three systems, to assess the stability and physical origin of these signals, and to search for short-period oscillations that may trace accretion dynamics or white dwarf rotation. Taken together, these datasets allow us to investigate variability over a wide range of timescales in these prototypical nuclear-powered systems. Our results suggest that such multi-timescale behavior is a prominent feature of this class of symbiotic binaries, reflecting the complex interactions inherent to their active phases.

2. OBSERVATIONS

Multi-wavelength optical photometric data, covering 14 years of observations from both space- and ground-based facilities, have been combined in this study. The complete observing log is presented in Table 1. We present the observations spanning a 14 yr observation period for AX Per, CI Cyg and Z And in Fig. 1, Fig. 7 and Fig. 13, respectively.

2.1. TUG Observations

We performed optical photometric observations of the objects with 60 cm (T60) robotic telescopes at TÜBİTAK National Observatory (TUG) in Türkiye. The observational period is between May 2019 and October 2024 by Bessel *U*, *B*, *V* and *R*-bands. The T60 data were reduced and analyzed using AstroImageJ (K. A. Collins et al. 2017), and differential photometry was performed using comparison stars in the CCD field.

The multicolor T60 photometry is used to construct the color–time diagram. Because the number of exposures obtained per night differs between bands, the data are nightly averaged in both brightness and time.

2.2. Observations by M. Sekeráš et al. (2019) (S19)

The objects were also observed by multicolor photometry at the Stará Lesná Observatory founded by the Astronomical Institute of the Slovak Academy of Sciences, as presented in M. Sekeráš et al. (2019) (hereafter S19). The observations² were performed using two Cassegrain telescopes with 60 cm and a Maksutov-Cassegrain telescope with 18 cm. The observational period of the data overlaps with half the period of the KWS data, and the T60 observations almost follow these observations. For all objects, observations with photometric uncertainties exceeding 0.5 mag were removed from the datasets.

2.3. ASAS-SN Observations

All-Sky Automated Survey for Supernovae (ASAS-SN; B. J. Shappee et al. 2014; C. S. Kochanek et al. 2017)³ is an optical sky survey observing by *V*-band. The objects were observed with the ba, bb, bc, and bd cameras at the Hawaii observatory (see Table 1). The ASAS-SN observations do not overlap temporally with the T60 data; however, the T60 monitoring began shortly after the ASAS-SN coverage ended.

2.4. KWS Observations

Kamogata/Kiso/Kyoto Wide-field Survey (KWS; H. Maehara 2014)⁴ is another program conducting observations in the *B*, *V* and *I_c*-bands. However, only a small amount of *B*-band data is available for the objects, particularly for AX Per and Z And. Observation dates in the KWS archive are provided in Gregorian calendar format; therefore, we convert them to Julian dates (JD) using an online converter tool⁵. The observational period for our objects spans a broader interval than that of the other missions and encompasses the epochs covered by ASAS-SN, S19, and T60. Consequently, we present over 13 yr of multi-wavelength optical photometry for all three objects.

2.5. TESS Observations

The Transiting Exoplanet Survey Satellite (TESS; G. R. Ricker et al. 2014) is a space-based observatory designed to obtain high-precision time-series photometry of individual targets across the entire sky. The Sector information of the objects is present in Table 1. All TESS data were retrieved from the Mikulski Archive for Space Telescopes (MAST) database⁶. Background-subtracted light curves were generated using the *TESSCut* (C. E. Brasseur et al. 2019) and *lightkurve Python* (Lightkurve Collaboration et al. 2018) packages. Postcard images were cropped to 11×11 pixels, and standard apertures were applied based on the point-spread function (PSF) results provided by *lightkurve*. Finally, flux time series were extracted for all targets. The observation windows are shown in the figures of the long-term light variations as vertical red bands.

TESS observations were acquired with different exposure times depending on the sector. Among the TESS data for our targets, the longest exposure corresponds to Sector 17 of the Z And system, with an exposure time of 1425 s (23.75 min). However, discrepancies were found between the downloaded data and the light curves produced using *TESSCut*. Inspection of the field image revealed that the source was located near the edge of the detector. Consequently, due to the unreliability of the data, observations from this sector were excluded from the analysis. Also, in Sector 84 of Z And, the corresponding light curve is not available in the database, likely because the target lies too close to the CCD edge, although the sector includes an observation of the source. Similar issues were encountered in some

² For data and their details cf. <https://www.astro.sk/caosp/Edition/FullTexts/vol49no1/pp19-66.dat/> and M. Sekeráš et al. (2019)

³ <https://asas-sn.osu.edu/>

⁴ <http://kws.cetus-net.org/~maehara/Vsdata.py>

⁵ <https://onlinetools.com/time/convert-date-to-julian-day>

⁶ <https://mast.stsci.edu/portal/>

sectors for all three systems. In Table 1, TESS observations used for this study are presented.

2.6. Gaia Observations

In Gaia Data Release 3 (DR3) (Gaia Collaboration et al. 2021), AX Per, CI Cyg and Z And is identified by ID409028569033785728, ID2047647756007944576 and ID1941894322438077312, respectively. Their distances are estimated using the parallax measurements from Gaia DR3 and the calculations by C. A. L. Bailer-Jones et al. (2021). Due to the variable nature of our sources, the geometric distances (r_{geo}) provided in the catalog were adopted instead of the photometric values. These distances are 2.112 ± 0.130 kpc, 1.943 ± 0.095 kpc 1.920 ± 0.079 kpc for AX Per, CI Cyg and Z And, respectively.

2.7. Frequency analysis of the observations

We have employed the *Lomb-Scargle periodogram* (N. R. Lomb 1976; J. D. Scargle 1982; J. T. Vander-Plas 2018) placed in the package of *astropy*⁷ to analyze the data of each band for each observatory. The Lomb-Scargle periodogram is a useful tool to process the irregular signals. Time-series analysis can provide more sensitive solutions in the analysis of data sets with irregular interruptions and non-uniform noise. The method operates by fitting sinusoid-like models to the data in order to compute the power spectrum of the frequencies. In this way, the amplitude distribution of periodic signals at different frequencies is obtained, allowing the identification of the most significant periodic components.

The peak point of the periodical signal can be represented by its probability and the peak height functions placed in *astropy*, defined as *false_alarm_probability()* and *false_alarm_level()*, respectively. For probability calculations, we adopt the statistical approach suggested by R. V. Baluev (2008).

A frequency analysis was performed for each observatory, applied sequentially across all photometric bands, because we have multi-band observations of several observatories. Though every mission has different resolutions, the signal strengths are five times higher than the background noise (J. D. Scargle 1982; J. H. Horne & S. L. Baliunas 1986; M. Zechmeister & M. Kürster 2009), meaning that the frequencies we obtained are significant at the 5σ level. We also present 3σ levels in the graphs in the necessary cases.

3. RESULTS

3.1. AX Per

3.1.1. Long-term light curve

A 14 yr observational period of AX Per is presented in Fig.1. AX Per is in an active phase during the entire monitoring period. Throughout this interval, the system exhibits high-amplitude outbursts, with *V*-band brightness increases of up to approximately 10 mag (see Fig.1). Three distinct brightness maxima brighter than 10.5 mag have been recorded. Deep and narrow minima are observed during this phase; however, after $\text{JD} \approx 2459000$ the eclipses become shallower, with increasing base brightness levels and broader minima showing low-amplitude wave-like behaviors.

Color-time diagram: At the beginning of the T60 observations, the system exhibits light contributions from both companions due to its orbital position. The light curve (Fig. 2) starts shortly after the maximum, showing a gradual decline in brightness. This period is associated with the system’s active phase. Between $\text{JD} \approx 2458640 - 2458880$, the system’s total luminosity decreases while its colors become progressively redder. This trend may indicate a diminishing contribution from the hot component and the associated ionized regions, particularly reflected in the decrease of the *U*-band flux.

After a gap in the observations, data starting around $\text{JD} \approx 2459000$ show bluer *U-B* and *B-V* colors. This interval corresponds roughly to the system’s eclipse minimum (indicated by the blue dashed lines in Fig. 1). Within $\text{JD} \approx 2458745 - 2459100$, a distinct hump-like brightening is detected, with the strongest amplitude in the *U* and *B* bands. The presence of this brightening despite the potential eclipse of the hot star suggests that a significant portion of the emission originates from the extended ionized nebula.

Following this phase, a sequence of small-amplitude, wave-like periodic variations is observed between $\text{JD} \approx 2459100 - 2459570$ (the periodical variation is ~ 37 and ~ 75 d). These brightenings show an inverse relationship between brightness and color, while the *V*-band brightens (or fades), the colors become redder (or bluer). Such behavior is observationally consistent with the variations typically originating from the cool giant, possibly due to pulsations, as also supported by similar fluctuations in the *R*-band. Comparable low-amplitude variations are also detected during $\text{JD} \approx 2459550 - 2460100$ and $\text{JD} \approx 2460460 - 2460550$.

At $\text{JD} \approx 2459570$, a noticeable fading is observed simultaneously in all filters, while the color indices remain nearly constant, consistent with the onset of an eclipse event. Around $\text{JD} \approx 2460090$, a prominent

⁷ <https://docs.astropy.org/en/stable/index.html>

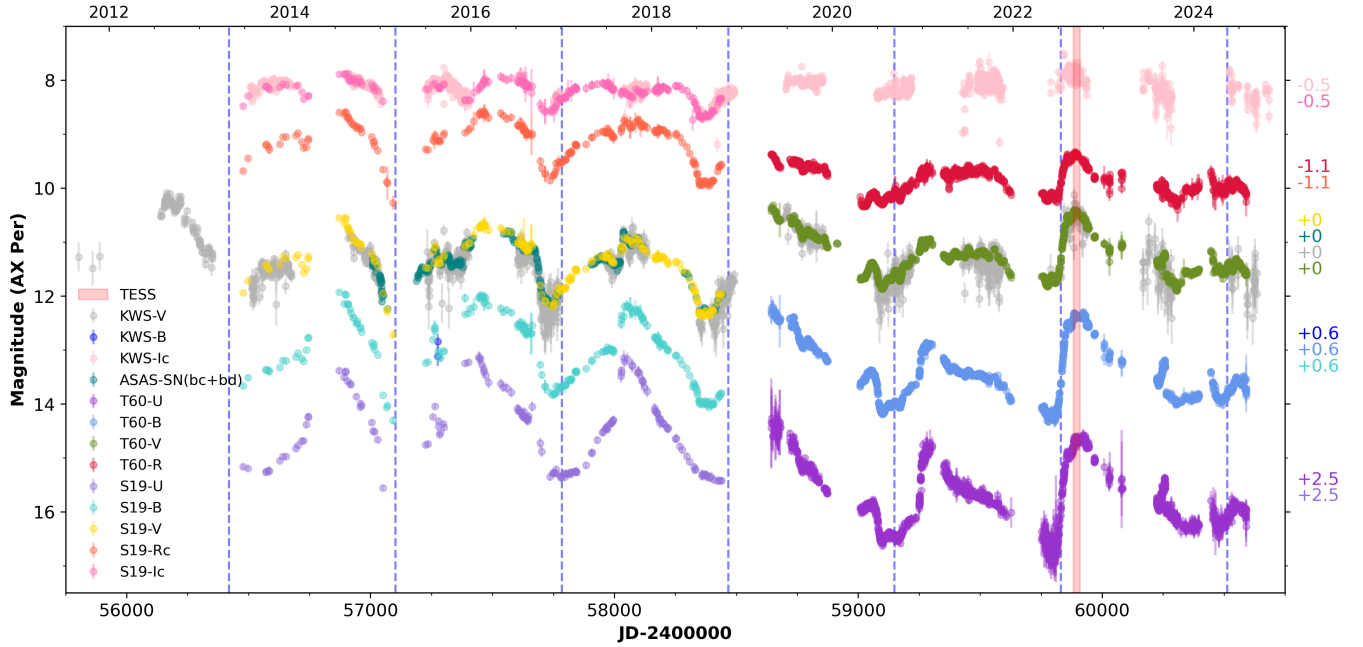


Figure 1. The light variations of all-bands data from ASAS-SN, KWS, S19 and T60 for AX Per. The red vertical bands span the TESS observation Sector(s), and the blue dashed lines correspond to the ephemeris of the inferior spectroscopic conjunction of the red giant according to F. C. Fekel et al. (2000a). The offset values with the same color codes are on the outside of the graph.

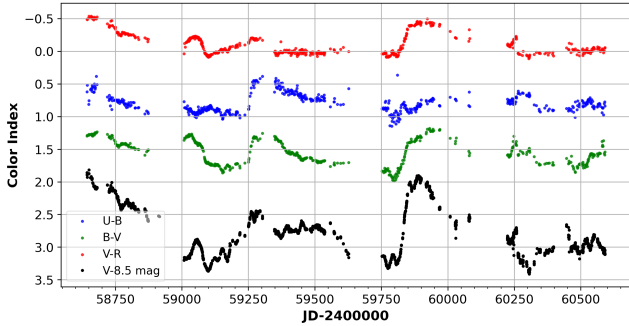


Figure 2. TUG T60 $U - B$, $B - V$ and $V - R$ colors for AX Per. T60 V -band is also shown by offset by -8.5 mag for easy comparisons with the colors.

brightening event dominates across all bands, with the strongest variations seen in the U and B filters. Between $JD \approx 2459820$ and 2460090 , the variations in these bluer bands are relatively small compared to other filters, suggesting that the outburst mainly manifests in the V -band. At the peak of the outburst, there were slight increases in both $U - B$ and $B - V$ values. Subsequently, the outburst declines, and the system begins to fade. During this fading phase, $U - B$ remains almost constant, with the brightness decreases without a significant change. This roughly 250 d long event is consistent with the characteristics of a *combination nova-type outburst*.

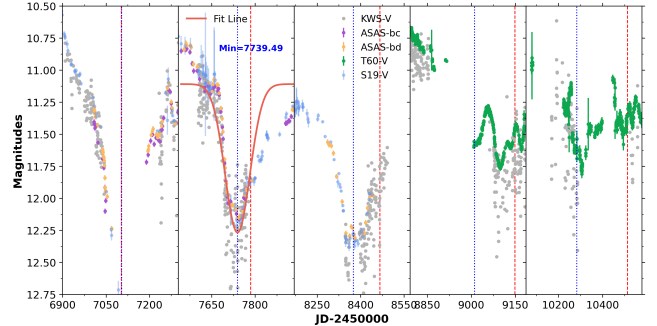


Figure 3. The expected minima locations for AX Per. The blue dotted lines indicate the positions of the observed minima based on the fit line, while the red dashed lines correspond to their positions calculated according to the ephemeris of F. C. Fekel et al. (2000a).

Around $JD \approx 246050$, a small-amplitude brightening is detected, followed by a sharp drop in brightness. This likely corresponds to a short outburst occurring just before the eclipse of the hot component, during which the brightening source begins to be obscured by the red giant ($JD \approx 2460260$).

Eclipsing Minima: During the observational period spanning more than 13 years, the system has reached its minimum brightness approximately 8 times. However, due to insufficient data coverage at certain epochs, only five intervals can be considered for the analysis of eclipse minima. This time interval to examine the

ephemeris of the orbitally related minima is inefficient and is additionally influenced by the intrinsic activity of the system. Rather than attempting to define the true orbital period, we here show how the lower limit of the observed minima varies and is influenced by the system’s activity, and compare our observed minima with the predicted dates from the spectroscopic ephemeris.

For the time interval with the densest coverage, a Gaussian fit was applied to determine the minimum, yielding $\text{JD} = 2457739.49$ (see the second panel from the left in Fig. 3). The fitting was performed over the range $2457545 < \text{JD} < 2457931$ using the combined KWS, S19, and ASAS-SN datasets. While the photometric uncertainties from KWS were included in the numerical analysis, they were omitted from the plotted figure for clarity. Using this minimum as a reference point and considering the 635.76 d periodicity derived from the V -band periodogram, the epochs of other eclipse minima were estimated. Afterward, we predicted dates from the spectroscopic ephemeris from [F. C. Fekel et al. \(2000a\)](#) ($\text{JD}_{\text{spec}} = 2450963.8(\pm 5.6) + 682.1(\pm 1.4) \times E$) and presented them with the red dashed lines on Fig. 3. This figure shows that determining the precise timing of the minima is particularly challenging, since AX Per exhibits outburst-like structures even during eclipse phases.

The wave-like fluctuations observed within the minima (such as those detected during the T60 observing intervals) further complicate these determinations. During quiescent phases, the dominant optical emission associated with the hot component and the nebula does not necessarily coincide with the center of mass of the hot star, while during strong outbursts, the region of enhanced emission may be closer to the hot component. As the system transitions between quiescent and active states, the dominant source of optical radiation shifts due to changes in the relative contributions of the hot companion and the surrounding nebula. This redistribution of the light-emitting regions leads to apparent displacements of the photometric minima, which do not reflect true variations in the orbital period but rather changes in the location of the system’s light center ([A. Skopal 1998](#)). This distinction helps to separate the stable orbital geometry of the system from the apparent shifts of the light centers that occur during active phases.

3.1.2. TESS observations

Photometric short-term variability of the three target systems was investigated using data obtained with the TESS. Only a single TESS sector is available for the AX Per system (Sector 57). The observation window

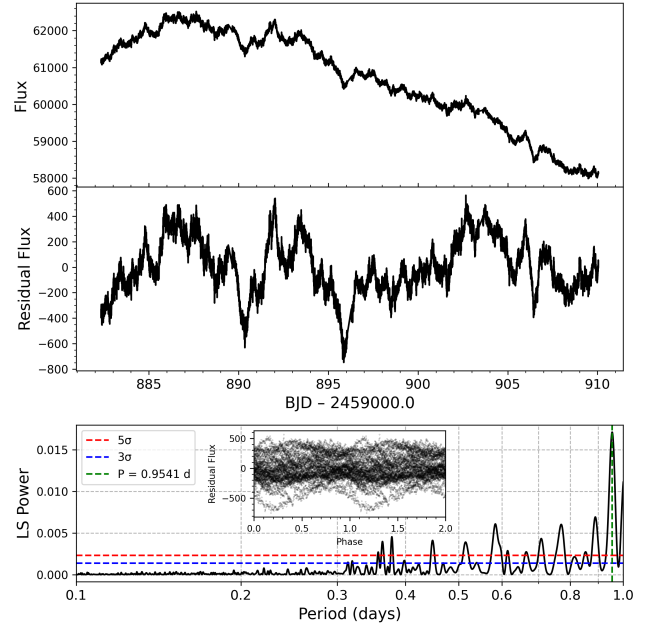


Figure 4. TESS observations and Lomb-Scargle Periodogram of AX Per. From top to bottom, the raw TESS light curve, the detrended light curve, and the periodogram of the detrended light curve with phase-folded light curve in the mini panel, respectively. At the bottom panel, the vertical green dashed line marks the period with the highest amplitude, shown correspond to the period of $P = 0.9541$ d ($f = 1.048 \text{ d}^{-1}$).

spans $2459882 < \text{BJD} < 2459910$. The TESS observations of AX Per are located at a phase where both components of the system are visible, and the brightness is at its post-eclipse maximum (see Fig. 1). The light curves used in this data correspond to the 120 s short-cadence mode, allowing us to probe variability on minute-level timescales with high photometric precision.

As seen in Fig. 4, throughout the sector, the flux exhibits a slight rise at the beginning of the observations, followed by a gradual decline. The light curve also displays short-term, flickering-like fluctuations (a photometric amplitude of about 200–400 electron s^{-1} in PDCSAP flux unit), a behavior not observed in the TESS data of the other systems. When the long-term light curve of the system is compared with the TESS timing window, it becomes evident that the TESS observed from near the peak of a broad till to the end of the hill-shaped maximum. To enhance the detectability of short-term variations in the periodogram and to remove the sector-long decreasing trend, the raw TESS light curve is fitted with a second-order polynomial across the sector, and this polynomial trend is subsequently subtracted from the data. The resulting detrended light curve is then analyzed using the Lomb–Scargle peri-

odogram. Here, we are interested in investigating the dominant frequencies in the range between 0.01 and 1 days.

3.1.3. Frequency analysis

The light curves of AX Per show the wave-like modulations following the main-brightness level with narrow amplitudes and small strengths of magnitudes (clearly seen in T60 observations). We investigate these variations and their characteristic parameters by frequency analysis. Additionally, we present all periodical frequencies obtained from the analysis (see Fig. 5).

T60 data. A significant modulation with a period of ~ 1213 d ($f = 0.00082$ d $^{-1}$) is detected in the *U*, *B*, and *V*-bands, although it is not the dominant signal. No corresponding variability is found in the *R* band, whereas in the *B*-band this frequency represents the strongest peak. The trend likely arises from the gradual decline in brightness observed over the monitoring interval, as the system appears brighter at the beginning of the *U* and *B*-band observations. Consequently, the closest frequency to the orbital period in these filters is found near 570 d ($f = 0.00175$ d $^{-1}$). The 1213 d signal affects the frequency analysis by distorting the dominant peak toward the orbital timescale. To correct for this, the long-term variation is modeled with a sinusoidal function and subtracted from the data before recomputing the periodogram. After detrending, the photometric periodicities of 646.97 d ($f = 0.00155$ d $^{-1}$) in the *U* band and 648.98 d ($f = 0.00154$ d $^{-1}$) in the *B*-band are recovered. In the *V*-band, a dominant frequency corresponding to a period of ~ 1216 d is also detected. However, removing this long-term variation does not affect the periodicity associated with the orbital cycle. Consequently, both the *V* and *R*-bands exhibit a consistent photometric periodicity of 648.98 d ($f = 0.00154$ d $^{-1}$). As noted in the previous section, determining the true orbital period of such systems from photometry alone is inherently challenging. In this study, rather than seeking the true orbital period, we aim to examine how the ephemeris derived from spectroscopic studies compares with the photometric minima obtained from our observations. The orbital period of 682.1 days reported from spectroscopic analyses of [F. C. Fekel et al. \(2000a\)](#) is approximately 40 days longer than the photometric period inferred here. As shown in Fig. 3, transitions between quiescent and active phases, together with wave-like fluctuations around the base of the minima, can naturally lead to discrepancies in the observed positions of the photometric minima. During quiescent phases, the dominant contribution to the optical emission arises from the extended ionized nebula, whose effective light

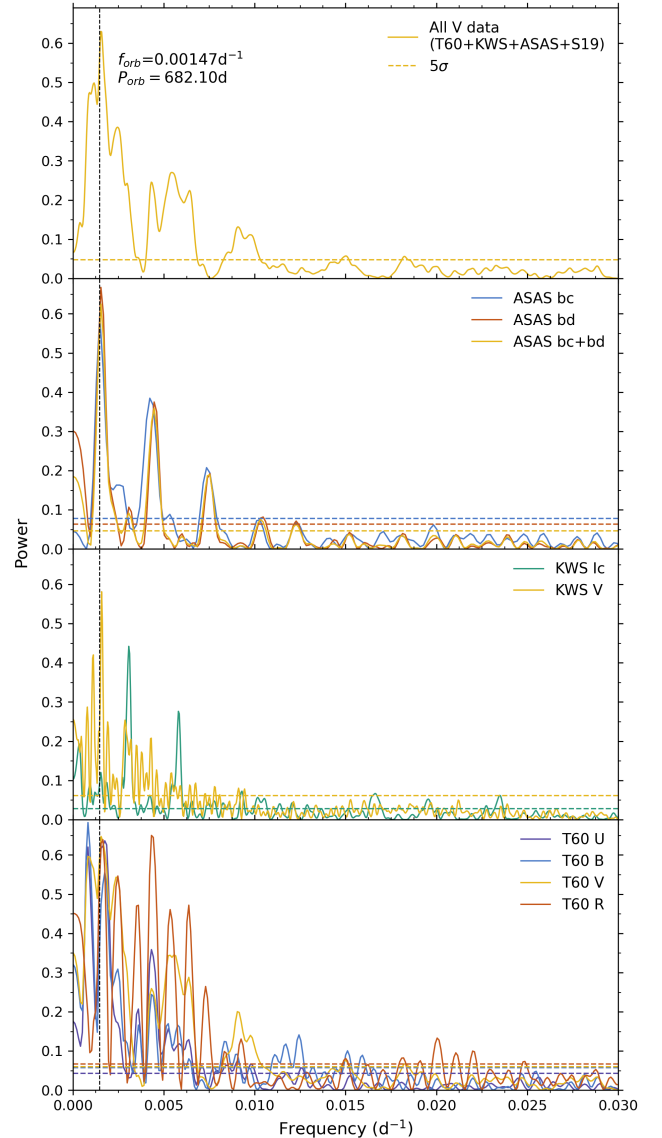


Figure 5. Lomb-Scargle Periodogram of AX Per for all observations. The vertical dashed line denotes the orbital frequency (f_{orb}) based on the spectroscopic period of [F. C. Fekel et al. \(2000a\)](#). The horizontal dashed lines, according to the color codes, indicate 5σ S/N levels of corresponding observations.

center does not coincide with the center of mass of the hot component. During active phases, the expansion of the hot component’s photosphere migrates the dominant region of optical emission closer to the hot component ([A. Skopal 1998](#)).

A dominant frequency around 230 d ($f = 0.0043$ d $^{-1}$) is detected in all photometric bands. This variation likely arises from the nearly periodic recurrence of outbursts and brightness peaks in the light curve, which occur on timescales of roughly 200–230 d. To better resolve lower-amplitude variations, the long-term

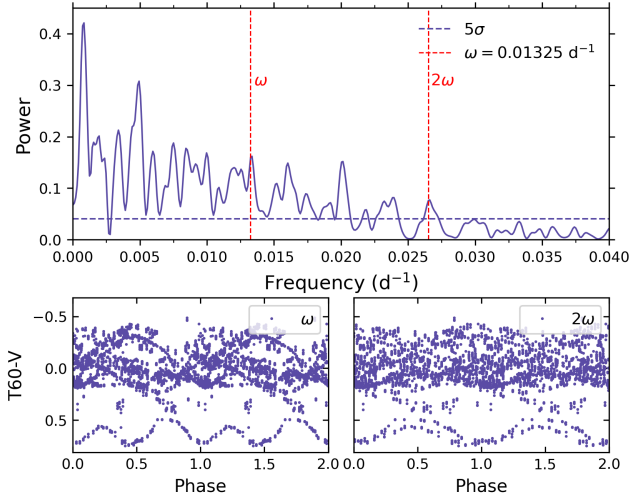


Figure 6. Upper panel: Power spectrum of the residual data after removing long-term sinusoidal variations. Lower Panel: Folded-phase diagrams of ω and 2ω from left to right, respectively.

modulations with periods of 1216 and 648.98 d are modeled with sinusoidal functions and subtracted from the dataset. After this correction, an “intermediate timescale” variation was identified, with periods of 75.82 ($f = 0.01319 \text{ d}^{-1}$), 76.05 ($f = 0.01315 \text{ d}^{-1}$), 74.88 ($f = 0.01335 \text{ d}^{-1}$), and 74.31 d ($f = 0.01346 \text{ d}^{-1}$) in the U , B , V , and R -bands, respectively. In addition, a secondary frequency corresponding to half of this period (~ 37.44 days; $f = 0.02671 \text{ d}^{-1}$) is also detected. The resulting periodogram and phase-folded light curves for these frequencies are shown in Fig. 6. The small-amplitude variations obtained for the V band correspond to periods of 37.73 d ($f = 0.02650 \text{ d}^{-1}$) and 75.46 d ($f = 0.01325 \text{ d}^{-1}$), which are in exact resonance with each other.

KWS data. The dominant frequency corresponding to the 1213 d variation detected in the T60 observations is also present in the KWS data. For the V -band, this strong pre-orbital signal corresponds to a period of 1271.49 d. The orbital period is determined to be 635.76 days ($f = 0.0016 \text{ d}^{-1}$) (see in Fig 5). The error sensitivity of the KWS data is lower than that of the other observatories. Meanwhile, this scattered dataset does not provide reliable results for detecting variations on the order of several tens of days. Nevertheless, after removing the higher-amplitude variations (1271.49 and 635.76 d) from the data, a low-amplitude periodicity of ~ 78.95 d ($f = 0.0127 \text{ d}^{-1}$) is identified in the V -band.

KWS observations are obtained in separate observing intervals, resulting in distinct clusters of data. For the V -band, these clusters typically span 170–200 d,

with gaps between them lasting about 200–230 days. During the frequency analysis, alias frequencies corresponding to these time intervals are identified. In the process of subtracting the dominant variations to isolate weaker signals, an additional modulation with a period of 210.08 d ($f = 0.00476 \text{ d}^{-1}$) is detected, which is interpreted as an alias frequency. In the I_c -band, the dominant frequency corresponds to a period of 321.2 d ($f = 0.0031 \text{ d}^{-1}$), close to a resonance with the orbital frequency. The second strongest signal appears at 171.13 d ($f = 0.0058 \text{ d}^{-1}$). It is important to note that KWS I_c -band data are conducted in discrete time segments, each lasting approximately 170 d, indicating that this frequency likely arises from the observing cadence and represents an alias. After the dominant variation is modeled with a sinusoidal function and subtracted from the dataset, a prominent frequency near the orbital period is identified, corresponding to 632.67 d ($f = 0.00158 \text{ d}^{-1}$). This variation is subsequently represented by a sinusoidal fit and removed, revealing an intermediate-timescale modulation with a period of 77.33 d ($f = 0.0129 \text{ d}^{-1}$).

ASAS-SN data. AX Per has been monitored by ASAS-SN over a time span of ~ 1434 d (3.93 yr). In the frequency analysis, data from all cameras is combined ($bc+bd$) to be analyzed together, after which the datasets from each camera are examined separately. The most prominent frequency detected in all cases corresponds to the orbital timescale, with periods of 651.83 d ($f = 0.00153 \text{ d}^{-1}$) for $bc+bd$, 680.66 d ($f = 0.00147 \text{ d}^{-1}$) for bc , and 651.82 d ($f = 0.00153 \text{ d}^{-1}$) for bd . The slight differences between cameras arise from the distinct durations of their observing baselines and, consequently, the number of covered orbital cycles. The bc camera, with a total monitoring span of about 1089 d, covers 2 eclipsing minima, whereas the bd camera, spanning 1434 d, samples 3 minima over ~ 2.2 orbital cycles.

All monitoring data. Additionally, we combine all V -band data of T60, KWS, and ASAS-SN to increase in data points. The predicted orbital period is obtained 635.76 d ($f = 0.0016 \text{ d}^{-1}$). After this variation is modeled with a sinusoidal function and subtracted from the dataset, an intermediate-timescale variation is measured as 75.26 d ($f = 0.0133 \text{ d}^{-1}$).

TESS data. We perform a period analysis of the TESS Sector 58 light curve of AX Per. A third-degree polynomial is fitted to the full dataset to remove long-term trends, and the analysis is carried out on the resulting detrended light curve. The highest-amplitude power in the periodogram lies between approximately 0.3 and 1 d. Periodicities shorter than 0.1 d fall well below the 3σ significance threshold and were therefore excluded

Table 2. The eclipse minima of CI Cyg determined from Gaussian fits to the T60 observations.

Bands	1. Primary Min.	2. Primary Min.
<i>U</i>	2458921.5689	2459779.6926
<i>B</i>	2458928.0150	2459787.0632
<i>V</i>	2458939.7697	2459802.2821
<i>R</i>	2458937.2872	2459804.9469

from further consideration. The most significant signal detected is a period of ~ 0.95 d (22.9 h), which may correspond to low-amplitude oscillations present in the light curve and is illustrated in Fig. 4. The phase-folded light curve exhibits a sinusoidal modulation. No shorter-period variability that could be associated with the white dwarf spin was identified.

3.2. CI Cyg

3.2.1. Long-term light curve

During ~ 14 yr observing interval analyzed, the system of CI Cyg predominantly exhibits quiescent-phase behavior (see Fig. 7). Within this interval, only a single pattern is detected in which the system’s brightness exceeds 10.5 mag (JD \sim 2456150). In fact, this indicates that the quiescent phase essentially begins following this outburst. Over the light variation, the system is characterized by low-energy, short-lived brightness fluctuations rather than sudden, high-energy outbursts throughout its quiescent state.

T60 data. CI Cyg was monitored with the TUG T60 telescope over a period of approximately 5.4 yr, covering about 2.3 orbital cycles. The light variations display clear wave-like fluctuations with low amplitudes, particularly in the *B*, *V*, and *R*-bands, where such modulations are evident along both the ingress and egress branches of the eclipses. To minimize the influence of such variations when determining the primary minima, the *U*-band data (being the least affected by these fluctuations) are used. Gaussian fits are applied to ~ 600 d data segments to estimate the times of minima. The resulting minima are $\text{JD}_{\text{minI}} = 2458921.5689$ and $\text{JD}_{\text{minII}} = 2459779.6926$, corresponding to a time interval of ~ 858.1237 d. Accordingly, the T60 photometric ephemeris is expressed as $\text{JD}_{\text{T60}} = 2458921.5689 + 858.1237 \times E$.

The ephemeris derived by A. Skopal et al. (2012) from eclipse observations is given as $\text{JD}_{\text{ecl.}} = (2441838.8 \pm 1.3) + (852.98 \pm 0.15) \times E$. There is a difference of 20.03 orbital cycles between the reference epoch (T_0) reported by A. Skopal et al. (2012) and the first minimum obtained from the T60 observations, corresponding to a phase shift of approximately 23.17 d. Considering the

orbital period of 852.98 d, this offset represents a deviation of about 2.7%. The primary minima determined for all photometric filters are listed in Tab. 2.

Color-time diagram. During the T60 monitoring, CI Cyg remain in a quiescent state; therefore, no sudden or intense outbursts capable of dominating the overall light variability are detected. The primary variability in CI Cyg is conventionally the orbital motion, while a secondary contribution arises from low-amplitude, wave-like brightness modulations with a characteristic period, similar to those identified in AX Per.

Fig. 8 presents the color diagram constructed from T60 multi-band photometric observations. The light curves display wave-like modulations that appear to vary with a characteristic timescale (see Sect. 3.2.3). While the *V*-band variability closely follows the behavior of the *V*–*R* color (with maxima and minima occurring simultaneously), the maxima in the *V*-band correspond to decreases in the *U*–*B* and *B*–*V* color indices, indicating an inverse color-magnitude relation. The fact that different color indices do not vary coherently suggests that these wave-like modulations cannot be straightforwardly attributed to a single source of variability. In particular, variations dominated purely by pulsations of the cool giant would be expected to produce more uniform color behavior. The observed color-dependent response may therefore reflect the blended contributions of the three basic radiation components in symbiotic systems (the cool giant, the hot star, and the ionized nebula), which are mixed within the photometric filters (U. Mürset et al. 1991; A. Skopal 2005). However, photometric data alone do not allow these contributions to be uniquely disentangled, and the underlying physical mechanism cannot be unambiguously identified on this basis.

Another noteworthy feature is the presence of wave-like modulations even during the eclipse of the hot component. While these variations are visible across all bands during the eclipse, the colors (particularly *V*–*R*) remain nearly constant. This suggests that the wave-like modulations are not directly associated with the hot component yet may instead arise from quasi-periodic pulsations of the red giant. The fact that these oscillations are most prominent in the *V* and *R*-bands, with only minor color changes, implies that the pulsation primarily modulates the system’s overall brightness. The wave patterns are especially pronounced in the *V* and *R*-bands, indicating that a quasi-periodic pulsation of the red giant is a likely origin. However, the lack of synchronicity among all color indices hints at a more complex process involving both pulsation and disk effects. Small-amplitude, quasi-periodic pulsations of the

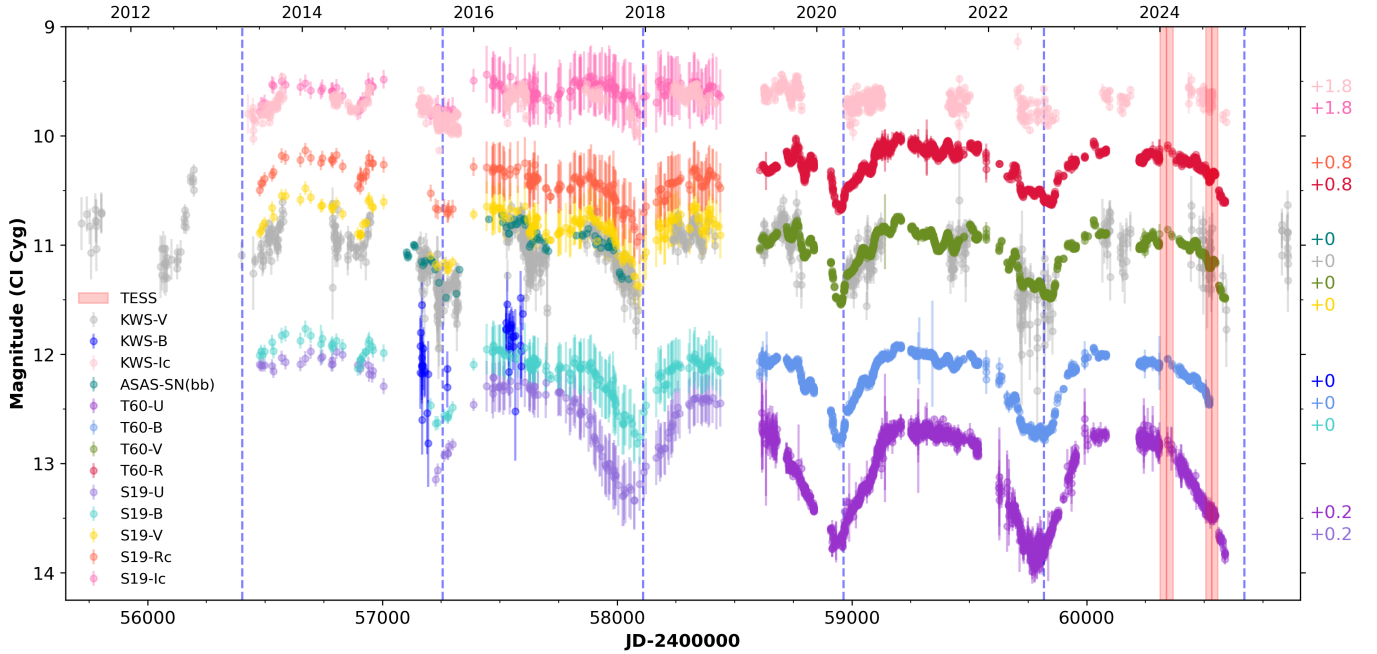


Figure 7. The light variations of all-bands data from ASAS-SN, KWS, S19 and T60 for CI Cyg. The red vertical bands span the TESS observation Sector(s), and the blue dashed lines correspond to the ephemeris referring to the inferior spectroscopic conjunction of the red giant according to F. C. Fekel et al. (2000b). The offset values with the same color codes are on the outside of the graph.

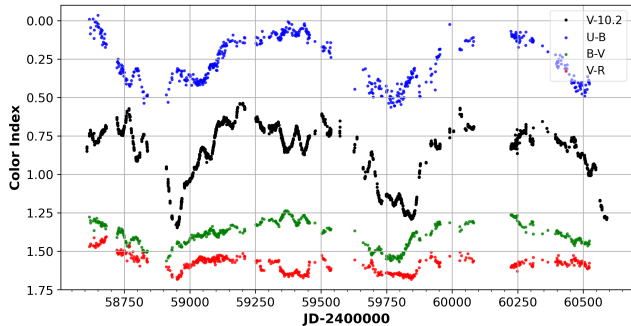


Figure 8. TUG T60 $U - B$, $B - V$ and $V - R$ colors for CI Cyg. T60 V -band is also shown by offset by -10.2 mag for easy comparisons with the colors.

red giant could produce the observed modulation in the V and R -bands, whereas the extended accretion disk of CI Cyg (S. J. Kenyon et al. 1991) may influence the hot-component radiation, leading to the inverse color behavior observed in $U - B$ and $B - V$.

3.2.2. TESS observation

CI Cyg is among the systems with the largest number of TESS observations, with data available from four separate TESS sectors. These observations correspond to Sector 74 ($2460312 < \text{BJD} < 2460339$), Sector 75 ($2460339 < \text{BJD} < 2460367$), Sector 81 ($2460506 < \text{BJD} < 2460533$), and Sector 82 ($2460533 < \text{BJD} < 2460559$). As shown in Fig. 7, the observations are dis-

tributed across the long-term light curve. The overall behavior of the long-term light curve is characterized by a decline from a peak-like maximum, superimposed with sinusoidal-like modulations. The behavior seen in the TESS light curves is not uniform when all sectors are combined into a single dataset. The first two sectors (Sectors 74 and 75) exhibit a Gaussian-like profile when merged, whereas the last two sectors (Sectors 81 and 82) display a more sinusoidal pattern. A second-order polynomial representation is applied to the four-sector light curve, bringing all segments to a consistent baseline (see Fig. 9). To identify both short- and long-term variations in the light curves, the Lomb-Scargle periodogram analysis is performed on all four sectors, as mentioned in the following section.

3.2.3. Frequency analysis

The frequency analysis shows that, across all filters, the dominant peak lies close to the orbital periodicity. Fig. 10 presents the power-frequency spectra derived from multiband photometry across all missions, with the dotted vertical line marking the frequency of the orbital period. The horizontal dashed lines in the power spectrum, color-coded by filter, indicate the 5σ significance threshold adopted for the detection of periodic signals.

T60 data. For the periodogram derived from the U -band of T60, the orbital period is measured as approximately 857.73 days ($f = 0.00117 \text{ d}^{-1}$). The period

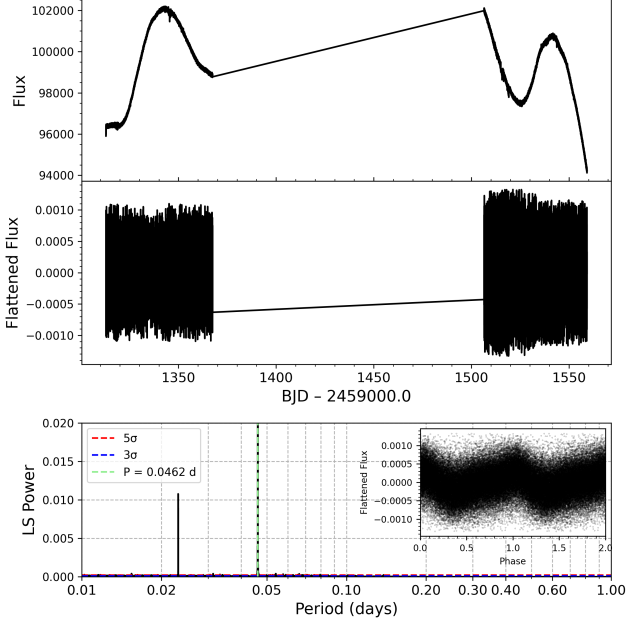


Figure 9. TESS data and Lomb-Scargle Periodogram of CI Cyg. From top to bottom, the raw TESS light curve, the flattened light curve (Savitzky-Golay filter), and the periodogram of the flattened light curve with phase-folded light curve in the mini panel, respectively. At the bottom panel, the vertical red dashed line marks the period with the highest amplitude, and the two peaks shown correspond to periods of $P = 0.0462$ d ($f = 21.65$ d $^{-1}$) and its first harmonic $P/2 = 0.0231$ d ($f = 43.29$ d $^{-1}$), right to left, respectively.

inferred from the power spectrum (857.73 d) is in excellent agreement with the 858.0287 d interval measured between the two eclipse minima in U -band.

After subtracting the large-amplitude variations from the T60 light curves using sinusoidal fits, a second frequency analysis was performed. The resulting dominant signals occur at $f = 0.01467$ d $^{-1}$ (68.17 d) in the U band, $f = 0.01342$ d $^{-1}$ (74.50 d) in both the B and V -bands, and $f = 0.01344$ d $^{-1}$ (74.39 d) in the R -band.

KWS data. In the frequency analysis of the KWS- I_c and V bands, the strongest peaks occur at $f = 0.00240$ d $^{-1}$ (416.76 d) and $f = 0.00234$ d $^{-1}$ (428.24 d), representing resonances of the orbital period. The fundamental orbital signal appears as the third-highest peak in the periodogram. When phased with the orbital period, the KWS light curves exhibit a clear secondary minimum, which is likewise evident in the T60 V - and B -band data Fig. 11. The orbital periods inferred from individual filters show slight variations, primarily due to discrepancies in the positions of these minima. Another prominent peak appears at $f = 0.00518$ d $^{-1}$ (192.95 d) in the KWS- I_c data and $f = 0.00514$ d $^{-1}$ (194.66 d) in the V -band. This periodicity is consistent with expect-

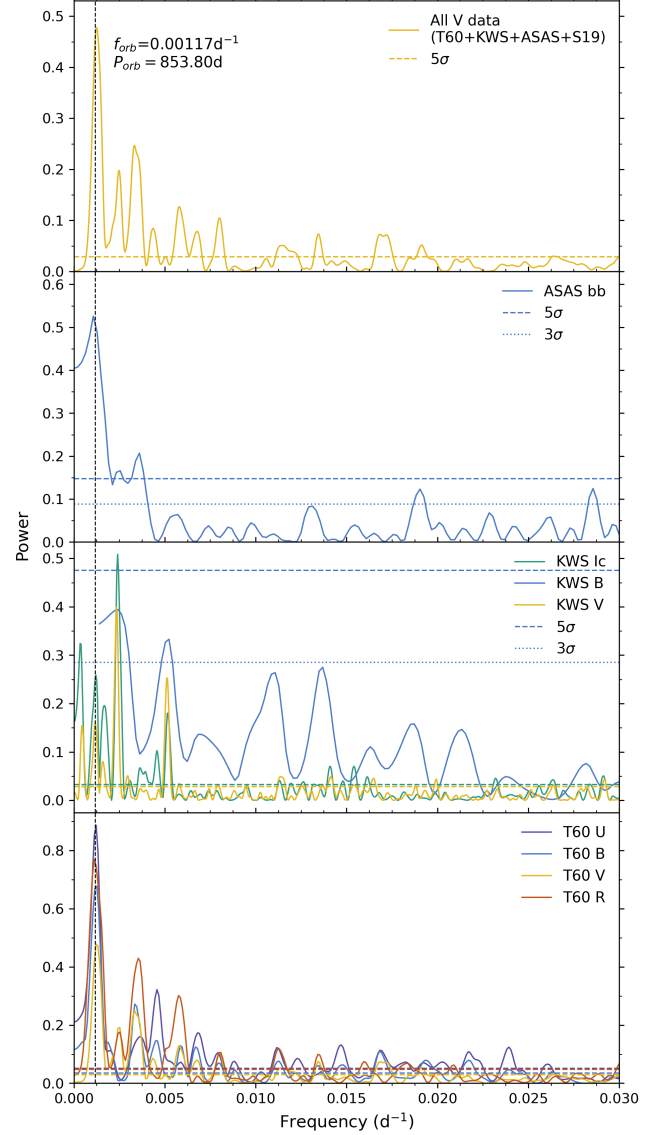


Figure 10. Lomb-Scargle Periodogram of CI Cyg for all observations. The vertical dashed line denotes the orbital frequency (f_{orb}) based on the spectroscopic period of [F. C. Fekel et al. \(2000b\)](#). The horizontal dashed and dotted lines according to the color codes indicate 5σ and 3σ significances of corresponding observations, respectively.

tations for pulsational variability of the red giant component.

The “intermediate-amplitude” variability of CI Cyg is apparent in nearly all observatories and across all photometric bands, though it is most clearly expressed in the V , R , and I_c filters (see Fig. 12). In the KWS data, the corresponding signals appear at $f = 0.01413$ d $^{-1}$ (70.78 d) in V and $f = 0.01411$ d $^{-1}$ (70.88 d) in I_c . In the ASAS-SN data, a comparable frequency of $f = 0.01311$ d $^{-1}$ (76.26 d) is detected.

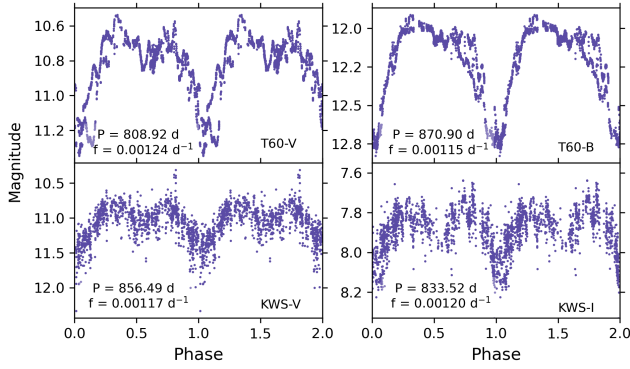


Figure 11. Phase-folded light curves of CI Cyg, computed using frequencies near the orbital period derived from the periodogram, showing pronounced secondary minima.

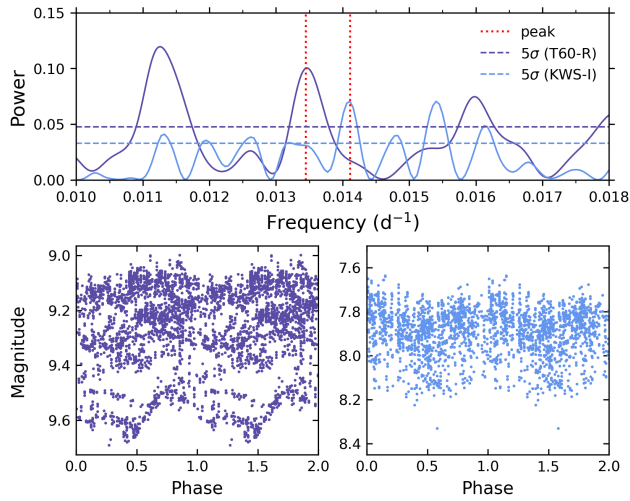


Figure 12. Upper panel: Power spectrum zoomed in the range of $0.010 - 0.018 \text{ d}^{-1}$ for near 70 d variations for T60- R and KWS- I_c . Lower Panel: Folded-phase diagram of $f = 0.01344 \text{ d}^{-1}$ and $f = 0.01411 \text{ d}^{-1}$ showed red dotted lines on the upper panel, left to right, respectively.

TESS data. The TESS analysis of CI Cyg is conducted using the combined light curves from four sectors. Compared to the high variability exhibited by AX Per, the light curve of CI Cyg is noticeably smoother and flatter. The data display sinusoidal variations with a characteristic timescale of approximately 40 days, which exceeds the duration of the individual sector observations. To isolate shorter-period signals, we remove trends longer than 1 day by detrending the light curve using the flatten routine implemented in the lightcurve package. This method applies Savitzky–Golay filtering with polynomial fits over prescribed windows, effectively normalizing the data and enhancing the visibility of short-timescale modulations. The Lomb–Scargle periodogram computed from the resulting detrended

light curve reveals a strong and dominant signal within the 0.01–0.1 d range. The most prominent period, 0.046229(6) d (66.57 min), along with its harmonics, appears across this frequency interval. The corresponding periodogram peaks and the phase-folded light curve at this period are presented in Fig. 9. The light curve folded on 66.57 min period displays a clear sinusoidal modulation.

3.3. Z And

3.3.1. Long-term light curve

The V -band photometric coverage of Z And spans roughly 13.2 yr. Fig. 13 presents the V -band data obtained from KWS, ASAS-SN, and T60, with the temporal window of the TESS observations highlighted by the red band. The KWS monitoring begins at a relatively bright epoch of the system ($\text{JD} = 2455777.2992$), when Z And is observed $V \approx 9$ mag. In the photometric study of A. Skopal et al. (2012), the onset of this outburst was captured, after which their observations concluded. The dataset presented in this work, together with the data of S19, therefore extends the photometric monitoring beyond the time span covered in that earlier study.

Over the 13 yr monitoring interval, the system exhibits a gradual decline of about one magnitude across two stages. A noticeable outburst occurs at $\text{JD} = 2455909.9269$, during which the brightness rises to $V \approx 8.8$ mag. This event subsequently fades to $V \approx 10.1$ mag over roughly 440 days. Between $2456351.9015 < \text{JD} < 2458107.878$, the system maintains a nearly steady brightness around $V \approx 10$ mag, with no major variability. A low-amplitude brightening appears to precede $\text{JD} \approx 2456860$, where the light curve shows the faint trailing signature of a decaying outburst.

A second major outburst is detected at $\text{JD} \approx 2458315.2$, observed first by ASAS-SN and subsequently by KWS, during which the brightness increases from 10.2 to 9.6 mag. A third major outburst occurs $\text{JD} \approx 2459066$, reaching a peak brightness of ~ 10.2 mag. As the system fades from this event, an additional low-amplitude brightening is observed, after which the system settles into a quiescent state.

Color-time diagram. The mean out-of-eclipse color index decreases over time. Within the interval $2458000 < \text{JD} < 2459500$, two consecutive large-amplitude outbursts and one smaller event are detected. Outbursts of this type are characteristic of Z And during its active phases (J. Merc et al. 2019). Throughout this period, the gradual decline in high-energy photon production is clearly visible in Fig. 14.

Examining the $U-B$ color around the outburst peaking at $\text{JD} \sim 2459066$ reveals that the event likely pro-

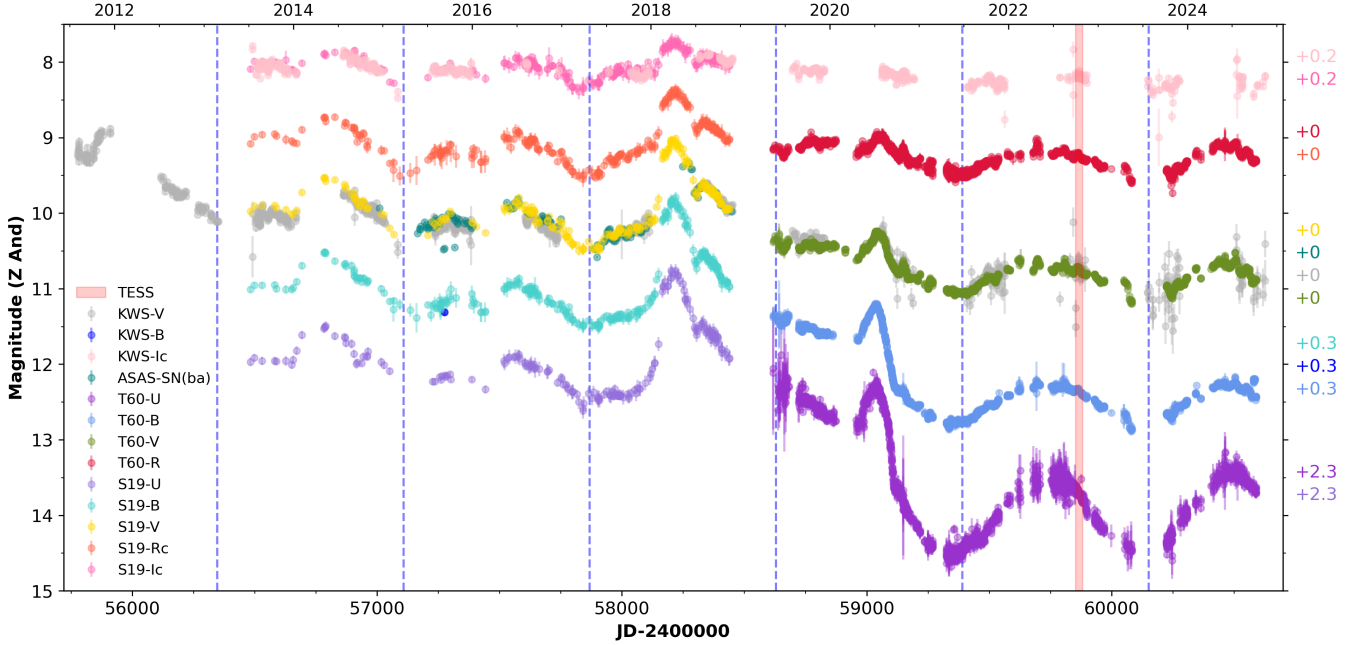


Figure 13. The light variations of all-bands data from ASAS-SN, KWS, S19 and T60 for Z And. The red vertical bands span the TESS observation Sector(s), and the blue dashed lines correspond to the photometric eclipsing minima obtained from $JD_{T60\&Fekel} = 2450260.2 + 760.85 \times E$ (see Sec. 3.3.3). The offset values with the same color codes are on the outside of the graph.

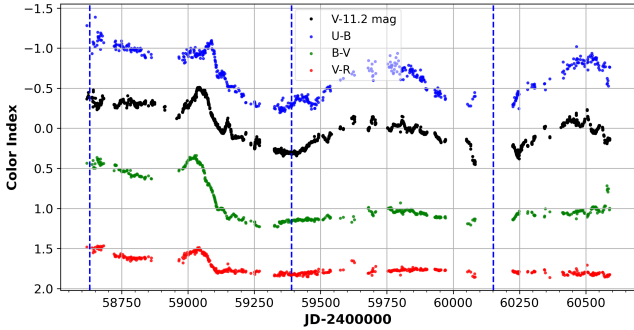


Figure 14. TUG T60 $U - B$, $B - V$ and $V - R$ colors for Z And. T60 V -band is also shown by offset by -11.2 mag for easy comparisons with the colors.

ceeds in two stages. As the outburst rapidly declines, a low-amplitude brightening (originating from the hot component) is observed $JD \sim 2459115$. Prior to the outburst, $U - B$ and $B - V$ become noticeably bluer. Subsequently, the contribution from ionized gas diminishes, and the flux at shorter wavelengths drops rapidly.

Fig. 14 marks the phases of the hot-component eclipse with blue dashed lines. Following the eclipse centered $JD \sim 2459390$, the $U - B$ color become a bluer lasting roughly 100 d. The fact that this enhancement appears in $U - B$ prior to any noticeable brightening in the V -band indicates that the increased energy production in the hot component first manifests through strengthened nebular emission. This rise in ionizing flux most likely

originates from localized activity within the inner accretion disk. The near constancy of the other color indexes suggests that the effect is spatially confined. Consequently, the event is consistent with a small-scale outburst driven by a local disk instability.

3.3.2. TESS observation

As in the case of AX Per, only a single TESS dataset is available for Z And. The observations cover the interval $2459853 < \text{BJD} < 2459882$ and correspond to the portion of the long-term light curve in which the system brightens toward a pronounced peak, followed by a rapid decline as the peak sharply subsides. In agreement with this overall behavior, the light curve of Sector 58 exhibits a trend suggesting that the observations capture a segment of a longer-period sinusoidal modulation, as illustrated in Fig. 15.

To extract the short-timescale variability and to enhance the signal amplitudes in the periodogram analyses, we detrend the full Sector 58 light curve using the flatten task defined in lightkurve. The light curve before and after detrending is shown in the top and middle panels of Fig. 15. The resulting residuals were then analyzed with periodograms to search for periodicities in the 0.01–1 d range. The corresponding power spectrum is presented in the bottom panel of Fig. 15.

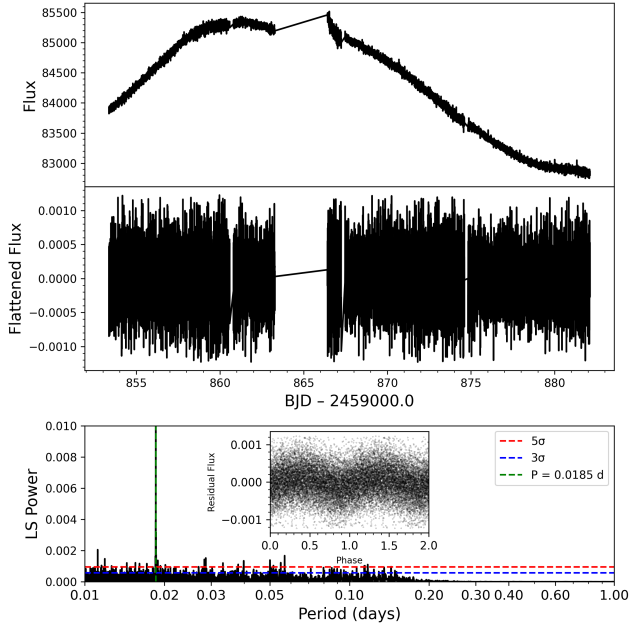


Figure 15. TESS photometry and Lomb-Scargle periodogram of Z And. From top to bottom, the background-corrected TESS light curve, the flattened light curve (Savitzky-Golay filter), and the periodogram of the flattened light curve are provided in order. The strongest peak reaches ~ 0.3 in amplitude at $P = 0.0185$ d ($f = 54.05$ d $^{-1}$), but the y-axis is limited to 0.01 for clarity.

3.3.3. Frequency analysis

A frequency analysis of the 13 yr photometric data of Z And yields a dominant signal ~ 800 d, which is larger than the expected orbital period. This offset arises from the system’s active-phase behavior, which introduces irregularities into the long-term light variations. To obtain a more reliable estimate of the orbital modulation, the frequency analysis was restricted to observations obtained after the system entered a quiescent state ($JD > 2459250$). Across all filters, a consistent and well-defined frequency of $f = 0.00131$ d $^{-1}$ (760.85 d) was identified.

Fig. 16 presents the resulting power spectrum for the quiescent interval, together with the phase-folded U -band light curve at the dominant frequency. The spectroscopic reference epoch $T_0 = 2450260.2$ from F. C. Fekel et al. (2000b) was adopted for phasing. The primary-minimum markers in Fig.14 correspond to the ephemeris $JD_{T60\&Fekel} = 2450260.2 + 760.85 \times E$.

M. Sekeráš et al. (2019) noted the presence of a ~ 58 d modulation in the AAVSO light curve of Z And. Here, we present the frequency analysis of the present data and provide further discussion of this signal. In our analysis of the full T60 data, we detect a clear peak at $f = 0.01704$ d $^{-1}$ (58.69 d) in the V -band and

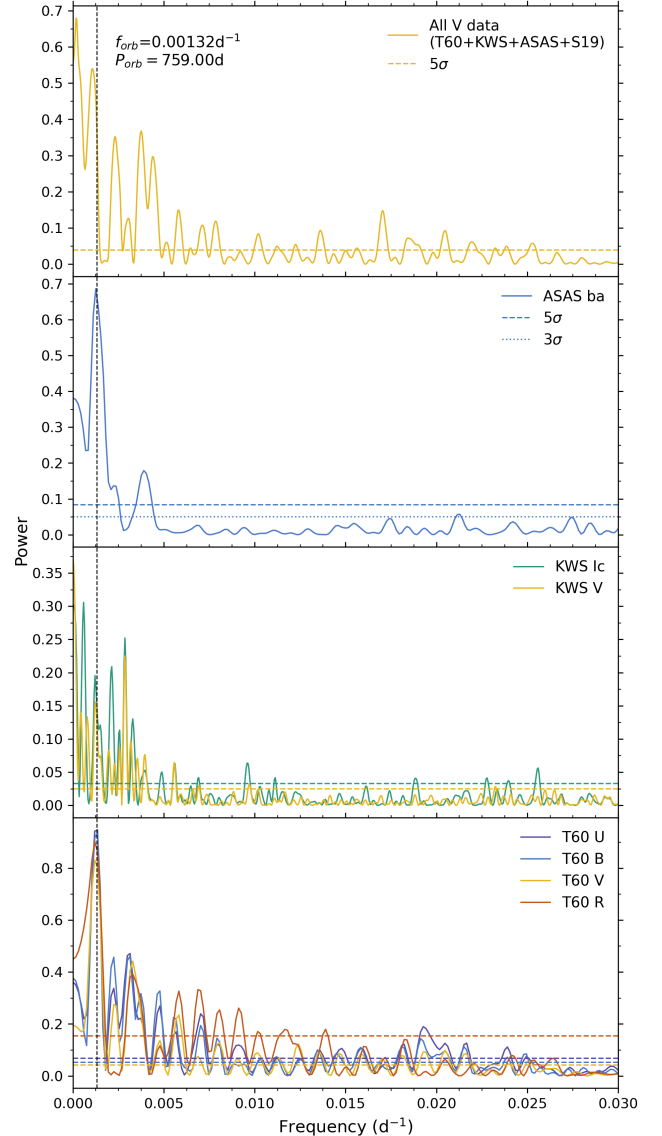


Figure 16. Lomb-Scargle Periodogram of Z And for all observations. The vertical dashed line denotes the orbital frequency (f_{orb}) based on the spectroscopic period of F. C. Fekel et al. (2000a). The horizontal dashed and dotted lines according to the color codes indicate 5σ and 3σ significances of corresponding observations, respectively.

$f = 0.01703$ d $^{-1}$ (58.71 d) in R -band. When the analysis is restricted to the quiescent interval, the characteristic timescale decreases slightly, yielding a period of ~ 55 d; the B -band data in this interval give $f = 0.01813$ d $^{-1}$ (55.15 d). Fig. 17 shows the corresponding power spectra and phase-folded light curves derived from both the full T60 interval and the quiescent-phase subset. The ASAS-SN data independently confirms this modulation, giving $f = 0.01744$ d $^{-1}$ (57.34 d). A quasi-periodic modulation with a characteristic timescale of ~ 58 days

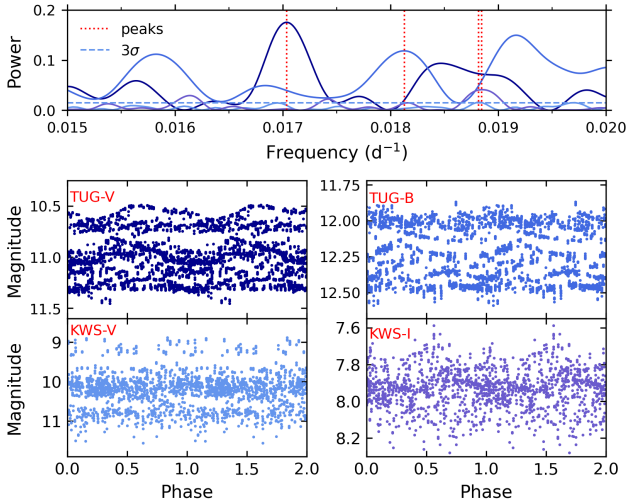


Figure 17. Top panel: Power spectrum zoomed in the range of 0.015 - 0.020 d^{-1} for around 55 d variations for Z And. Lower Panel: The light curves folded by related peak frequencies (see text for details).

becomes prominent across all filters and color indices during the quiescent phase.

Although 55–60 d modulation is less pronounced in the KWS- V and I_c datasets, the dominant peaks occur at $f = 0.01885 \text{ d}^{-1}$ (53.06 d) and $f = 0.01882 \text{ d}^{-1}$ (53.15 d), respectively (see bottom panel of Fig. 17). The longer and more irregular sampling of the KWS observations causes the apparent period to change slightly. Moreover, because Z And is in an active state during roughly 70% of the KWS coverage, the modulation is significantly diluted by outburst-related variability.

The phase-folded KWS- V light curve shows that the system occupies three distinct brightness levels. This multi-level behavior corresponds to the step-like transition from the active to the quiescent state seen in the long-term light curve (Fig. 13). In the inner graph of the left-bottom panel of Fig. 17, ~ 53 d modulation is more clearly visible during the quiescent interval, when the brightness remains within the 11–10.5 mag range.

Taken together, both the active- and quiescent-state data reveal a semi-periodic modulation. Its enhanced visibility at lower energies and its behavior in the color–time diagrams strongly suggest that this variability arises from non-radial, semi-periodic pulsations of the red giant component.

TESS data. Z And exhibits a smooth and relatively stable light curve in TESS observations, similar to that of CI Cyg. The overall trend indicates that the observations capture a portion of a sector-long, sinusoid-like modulation. After detrending the data, the Lomb–Scargle periodogram reveals a frequency of

0.01854(2) d (26.7 min), detected within the 0.01–0.1 d interval and accompanied by several harmonics. The light curve folded on this period displays a clear sinusoidal modulation, as presented in Fig. 15.

4. DISCUSSION

This study presents a comprehensive 13 yr photometric analysis of the symbiotic systems AX Per, CI Cyg, and Z And, combining long-term TUG T60 multicolor observations with additional public data sets. T60 observations, which provide the most continuous and highest-quality data within this study, enable the identification of both large-amplitude outbursts and subtle low-amplitude variations occurring on a range of timescales. Given that SySts contain astrophysical components spanning a wide temperature range, including a cool giant, a hot compact object, and an extended ionized nebula, multicolor photometry is essential for diagnosing the physical origin of observed brightness variations. Below, we summarize the physical interpretations of variability for each system and place them in context with earlier results in the literature.

AX Per has been in an active stage since mid-2007, consistent with the behavior reported by A. Skopal et al. (2011). Their observations ended in 2011, whereas the data analyzed here extend from mid-2011 to the end of 2023, effectively continuing the monitoring of the same active phase. Throughout the entire ~ 13 yr timespan, the system remained active. During the active phase, AX Per exhibits narrow and deep minima. However, starting around $\text{JD} \sim 2459000$, both the depth and width of minima begin to change, showing shallower and broader profiles. The presence of low-amplitude wave-like fluctuations during eclipses clearly disrupts the originally sharp eclipse shape. In quiescence, AX Per is known to exhibit broad minima due to the dense, optically thick ionized wind of the red giant, modulated by orbital motion (A. Skopal et al. 2001). During quiescence, the accretion disk gradually re-forms, leading to the transformation of V-shaped minima into broad structures. A. Skopal et al. (2011) argued that the 2007–2010 active phase was driven by a significant brightening of the hot component. They modeled the changing eclipse shapes by suggesting that the white dwarf wind accumulates preferentially near the equatorial plane, creating a disk-like structure. This structure reprocesses radiation from the hot component and contributes significantly to the optical brightness. Our T60 multicolor data confirm that AX Per remains notably blue, with average colors $U - B \approx 0.75$, $B - V \approx 1.5$, and $V - R \approx -0.2$, consistent with hot-component-dominated emission during this continued active stage.

Table 3. Summary of long-, intermediate-, and short-term variability in three symbiotic stars. The Interpretation column lists the possible physical origins corresponding to the long, intermediate, and short modulations, respectively. Here, EM: eclipse-modulated variability; QPO: quasi-periodic oscillation; WD: white dwarf.

Name	Long	Intermediate (30-200 d)	Short	Interpretation
AX Per	~640 d	75 d & 37.7	~0.95 d	EM; Non-radial puls. & its harmonic; QPO
CI Cyg	~855 d	~74 d	~66.6 min	EM; Disk+red giant puls.; Possible WD Spin
Z And	~759 d	~58.7 d	26.7 min	EM; Accretion-driven variability; WD spin

Orbital period determinations vary across data sets and epochs. While the quiescent-state orbital period is known to be ~ 680 d, our combined multi-observatory analysis yields ~ 635 d, and the T60 data alone give ~ 648.5 d. Systems such as AX Per are known to exhibit apparent changes in the orbital period, manifested as displacements in the timings of photometric minima caused by changes in the spatial distribution of the dominant optical emission, particularly within the ionized nebula, rather than by true orbital evolution (A. Skopal 1998). In active systems, additional structural complexity (e.g., circumstellar material) may further affect the observed minima. Although differences of several days may appear large in the time domain, they correspond to relatively small offsets in frequency space ($\sim 10^{-4} \text{ d}^{-1}$) and are typical of nebula-embedded long-period symbiotic binaries. Thus, the main goal here is not to refine the orbital period but to understand the physical mechanisms responsible for the apparent changes in minimum locations. A striking result from the T60 data is the detection of stable wave-like modulations at 75.46 d and its harmonic 37.73 d. These resonant periods are best explained by non-radial, semi-regular pulsations of the red giant, consistent with expected pulsation ranges of 40–200 d for S-type symbiotics (J. Merc & H. M. J. Boffin 2025). Such multimode pulsations, possibly modulated by disk instabilities or orbit–pulsation interactions (E. M. Leibowitz & L. Formigini 2008; K. H. Hinkle et al. 2019), also reproduce the color behaviors observed here: brightness increases while colors redden (or vice versa), indicating cool-component variability. All evidence points toward strong, non-radial pulsations of the giant as the primary source of these modulations.

The long-term variability of CI Cyg shows a prominent quasi-periodic modulation around ~ 70 –74 d, with sinusoidal morphology and noticeable amplitude and phase drifts. These low-amplitude variations are strong enough to obscure the primary eclipse minima, making the determination of precise eclipse timings difficult. Despite the similarity to red giant pulsations, CI Cyg shows phase-reversed behavior in some colors, implying that more than one physical process may be operating. Earlier observations by S. J. Kenyon (1982) reported

low-amplitude (0.1–0.3 mag) modulations during eclipse minima, demonstrating that this variability cannot be solely attributed to pulsations or shell burning. Spectroscopic data further suggest contributions from ionized gas structures surrounding the system. If the accretion disk is geometrically larger than the giant at orbital conjunction, the far rim of the disk may remain visible even during eclipse, allowing disk-intrinsic variability to appear as out-of-eclipse-like brightness modulation. For this effect to be strong, the disk must contribute significantly to the UV/optical brightness, consistent with the presence of a hot, optically thin disk during quiescence (J. Mikolajewska 1996). Given the system’s moderately eccentric orbit ($e = 0.15 \pm 0.08$, $i = 73^\circ \pm 6^\circ$; S. J. Kenyon et al. 1991), the disk is unlikely to be homogeneous. Non-uniform mass loading from the giant’s wind could naturally produce density waves propagating through the disk, which in turn modulate the emission from the ionized nebula. These considerations support a hybrid interpretation: the ~ 74 d variability likely arises from a combination of red giant pulsations and structural/ionization changes within the disk–nebula environment. T60 data show a gradual decline in the modulation amplitude after the second eclipse, consistent with the idea that activity-triggered structural changes from past outbursts may be relaxing. Continued monitoring (especially with spectroscopy) is required to disentangle these contributions.

Across the ~ 13 yr dataset, Z And exhibits behavior characteristic of an active system, consistent with long-term activity reported since 2000.7 (A. Skopal et al. 2012). After the brightening around JD ~ 2459066 , the system began to show broad, orbitally modulated variations similar to quiescent stages, with magnitudes ranging between $V = 10.5 - 11$. However, as emphasized by M. Sekeráš et al. (2019), Z And can mimic quiescent-like morphology even during active states, making continued observations essential. Z And is known to display variability from minutes to tens of days. In our T60 analysis, a periodicity near 58.69 d is detected, consistent with the ~ 58 d modulation noted in AAVSO V -band observations by M. Sekeráš et al. (2019), although they did not explore the origin of this behavior. Our frequency

analysis confirms the stability of this timescale, but the physical origin remains unclear. It may relate to quasi-periodic mass-transfer fluctuations, thermal–viscous instabilities, or pulsation-modulated wind variability.

Although not the primary focus of this study, we also present the short-period variations (<1 d) identified in the TESS data, which provide a broader context for interpreting the intermediate-timescale variability of the systems. Detecting short-term variability in SySts requires intensive, multi-color, and preferably continuous overnight observations. Measuring these rapid changes coherently across different energy ranges is essential, as they may be linked to the rotation of the white dwarf. From this perspective, one of the best-characterized systems with a confirmed white dwarf spin period is FN Sgr, where a period of 11.3 min has been reported (J. Magdolen et al. 2023). However, the long orbital periods and strong intrinsic variability typical of symbiotic binaries make the detection of coherent spin signals particularly challenging.

We note that the 26.7 min modulation detected in TESS data of Z And is consistent with the expected spin-related variability of the accreting white dwarf. This interpretation is strongly supported by the earlier discovery of a persistent ~ 28 min optical oscillation by J. L. Sokoloski & L. Bildsten (1999), detected on all observing nights over nearly one year. The close agreement between the two periods suggests a common physical origin, now observed in space-based photometry with improved precision and continuous temporal coverage. In addition, for CI Cyg, we detect a 66.6 min modulation that may plausibly be associated with white dwarf spin. Nonetheless, periodicity of this kind could also arise from plasma motions in the innermost accretion regions, and distinguishing between these scenarios remains nontrivial. For this reason, we strongly recommend dedicated nightly follow-up observations to verify the stability and coherence of the detected frequency. J. Merc et al. (2024) reported several findings based on TESS observations of some symbiotic stars. Although our analysis employs different methods, these results remain consistent with their conclusions.

In AX Per, we identify a signal near ~ 0.95 d (22.9 h). Although some cycles of the folded light curve show recognizable structures at this period, the absence of a consistently repeating pattern across all cycles suggests that the variability may be quasi-periodic rather than strictly coherent. Comparisons with magnetic systems such as intermediate polars among cataclysmic variables indicate that confirmed white dwarf spin periods are typically much shorter than one day (D. de Martino et al. 2020). However, symbiotic systems exhibiting compar-

atively long spin periods do exist; for example, BF Cyg shows a modulation of ~ 1.8 h (L. Formigini & E. M. Leibowitz 2009), indicating that extended rotation periods are within the observed range for this class of objects.

Taken as a whole, our results show that AX Per, CI Cyg, and Z And all display photometric variability spanning several distinct timescales. In each system, long-term activity, intermediate-period modulations, and shorter-period signals are present simultaneously, yet remain clearly separated in period space. Although the observational characteristics of these variations have now been identified, their physical origin and possible interconnections are not immediately evident. In the next section, we therefore examine these results in a broader physical context, considering the roles of red-giant pulsations, accretion-related phenomena, and the overall structure of symbiotic binary systems.

5. CONCLUSION

The three systems display a rich hierarchy of variability spanning timescales from minutes to years. While the long-term behavior is governed by orbital modulation and outburst activity, all targets exhibit persistent intermediate-timescale oscillations with periods between 30 and 100 days. These signals appear consistently across independent datasets, persist through both active and quiescent states, and reach amplitudes of up to 0.25 mag. Their presence in all three systems points to a common physical origin, potentially involving large-scale variations in the red-giant wind, magnetically influenced accretion structures, or quasi-periodic density enhancements at the wind–accretor interaction interface.

The observed periods fall outside the range of the fundamental and overtone radial pulsations expected for M giants, yet they are naturally compatible with semi-regular or non-radial pulsation modes of the cool component. Such pulsations may lead to time-dependent variations in the mass-loss rate from the red giant and, consequently, to transient enhancements in the accretion rate onto the white dwarf. This scenario provides a plausible framework linking intermediate-timescale variability to the triggering of Z And-type outbursts, although a direct causal connection has not yet been observationally demonstrated. In AX Per and CI Cyg, the persistence of 37–75 d signals across multiple studies indicates a long-lived and possibly stable process. In Z And, the ~ 58 d modulation, now confirmed independently, demonstrates that such intermediate-timescale variability is a robust and intrinsic component of symbiotic mass transfer.

High-cadence TESS photometry provides compelling evidence for short-period variability in these systems. The 26.7 min modulation in Z And and the 66.6 min signal in CI Cyg remain phase-coherent over multiple sectors, supporting interpretations involving white dwarf spin or magnetically gated accretion. The weak 0.95 d signal in AX Per is confined to quiescent intervals and therefore requires independent verification. Together, these detections show that the hot components of symbiotic binaries can sustain stable or quasi-stable rotational or accretion-driven oscillations that are accessible only through continuous space-based monitoring.

Taken together, our results support the view that intermediate-timescale photometric variations on the order of tens of days are a recurrent and physically significant component of variability in shell-burning symbiotic binaries. Future multiwavelength campaigns that combine optical photometry, UV spectroscopy, and hydrodynamical modeling will be essential to determine whether the dominant mechanism arises from pulsation, wind-structure variations, or accretion-related instabilities. Extending the analysis to additional symbiotic

systems observed by TESS will further clarify whether these modulations are truly widespread.

ACKNOWLEDGMENTS

The authors thank the anonymous referee for their constructive comments and valuable suggestions, which significantly improved the quality of this manuscript. This study was supported by the Scientific and Technological Research Council of Türkiye (TÜBİTAK) under Grant Number 124F073. The authors thank TÜBİTAK for their support. We thank TÜBİTAK National Observatory (TUG) for partial support in using T60 telescope with project number 19BT60-1495. This article includes a part of the PhD thesis of M.Y.

Facilities: TUG T60: 60cm, ASAS-SN, KWS, TESS, Stará Lesná Observatory, Gaia

Software: astropy (Astropy Collaboration et al. 2013, 2018, 2022), AstroImageJ (K. A. Collins et al. 2017), LombScargle (J. D. Scargle 1982; J. T. VanderPlas 2018), lightkurve (Lightkurve Collaboration et al. 2018), TESSCut (C. E. Brasseur et al. 2019)

REFERENCES

- Astropy Collaboration, Robitaille, T. P., Tollerud, E. J., et al. 2013, *A&A*, 558, A33, doi: [10.1051/0004-6361/201322068](https://doi.org/10.1051/0004-6361/201322068)
- Astropy Collaboration, Price-Whelan, A. M., Sipőcz, B. M., et al. 2018, *AJ*, 156, 123, doi: [10.3847/1538-3881/aabc4f](https://doi.org/10.3847/1538-3881/aabc4f)
- Astropy Collaboration, Price-Whelan, A. M., Lim, P. L., et al. 2022, *ApJ*, 935, 167, doi: [10.3847/1538-4357/ac7c74](https://doi.org/10.3847/1538-4357/ac7c74)
- Bailer-Jones, C. A. L., Rybizki, J., Fouesneau, M., Demleitner, M., & Andrae, R. 2021, *VizieR Online Data Catalog*, I/352
- Baluev, R. V. 2008, *MNRAS*, 385, 1279, doi: [10.1111/j.1365-2966.2008.12689.x](https://doi.org/10.1111/j.1365-2966.2008.12689.x)
- Belczyński, K., Mikołajewska, J., Munari, U., Ivison, R. J., & Friedjung, M. 2000, *A&AS*, 146, 407, doi: [10.1051/aas:2000280](https://doi.org/10.1051/aas:2000280)
- Bollimpalli, D. A., Hameury, J.-M., & Lasota, J.-P. 2018, *MNRAS*, 481, 5422, doi: [10.1093/mnras/sty2555](https://doi.org/10.1093/mnras/sty2555)
- Brasseur, C. E., Phillip, C., Fleming, S. W., Mullally, S. E., & White, R. L. 2019, *Astrocute: Tools for creating cutouts of TESS images*, Astrophysics Source Code Library, record ascl:1905.007 <http://ascl.net/1905.007>
- Collins, K. A., Kielkopf, J. F., Stassun, K. G., & Hessman, F. V. 2017, *AJ*, 153, 77, doi: [10.3847/1538-3881/153/2/77](https://doi.org/10.3847/1538-3881/153/2/77)
- de Martino, D., Bernardini, F., Mukai, K., Falanga, M., & Masetti, N. 2020, *Advances in Space Research*, 66, 1209, doi: [10.1016/j.asr.2019.09.006](https://doi.org/10.1016/j.asr.2019.09.006)
- Fekel, F. C., Hinkle, K. H., Joyce, R. R., & Skrutskie, M. F. 2000a, *AJ*, 120, 3255, doi: [10.1086/316872](https://doi.org/10.1086/316872)
- Fekel, F. C., Joyce, R. R., Hinkle, K. H., & Skrutskie, M. F. 2000b, *AJ*, 119, 1375, doi: [10.1086/301260](https://doi.org/10.1086/301260)
- Formigini, L., & Leibowitz, E. M. 1990, *A&A*, 227, 121
- Formigini, L., & Leibowitz, E. M. 1994, *A&A*, 292, 534
- Formigini, L., & Leibowitz, E. M. 2009, *MNRAS*, 396, 1507, doi: [10.1111/j.1365-2966.2009.14835.x](https://doi.org/10.1111/j.1365-2966.2009.14835.x)
- Gaia Collaboration, Brown, A. G. A., Vallenari, A., et al. 2021, *A&A*, 649, A1, doi: [10.1051/0004-6361/202039657](https://doi.org/10.1051/0004-6361/202039657)
- Hinkle, K. H., Fekel, F. C., Joyce, R. R., et al. 2019, *ApJ*, 872, 43, doi: [10.3847/1538-4357/aafba5](https://doi.org/10.3847/1538-4357/aafba5)
- Horne, J. H., & Baliunas, S. L. 1986, *ApJ*, 302, 757, doi: [10.1086/164037](https://doi.org/10.1086/164037)
- Kato, M., & Hachisu, I. 2023, *ApJ*, 951, 128, doi: [10.3847/1538-4357/acdb4c](https://doi.org/10.3847/1538-4357/acdb4c)
- Kenyon, S. J. 1982, *PASP*, 94, 165, doi: [10.1086/130957](https://doi.org/10.1086/130957)
- Kenyon, S. J. 1986, *The symbiotic stars* (Cambridge University Press), doi: [10.1017/CBO9780511586071](https://doi.org/10.1017/CBO9780511586071)
- Kenyon, S. J., Oliverson, N. A., Mikołajewska, J., et al. 1991, *AJ*, 101, 637, doi: [10.1086/115712](https://doi.org/10.1086/115712)

- King, A. R., & Pringle, J. E. 2009, *MNRAS*, 397, L51, doi: [10.1111/j.1745-3933.2009.00682.x](https://doi.org/10.1111/j.1745-3933.2009.00682.x)
- Kochanek, C. S., Shappee, B. J., Stanek, K. Z., et al. 2017, *PASP*, 129, 104502, doi: [10.1088/1538-3873/aa80d9](https://doi.org/10.1088/1538-3873/aa80d9)
- Leibowitz, E. M., & Formiggin, L. 2008, *MNRAS*, 385, 445, doi: [10.1111/j.1365-2966.2008.12847.x](https://doi.org/10.1111/j.1365-2966.2008.12847.x)
- Lightkurve Collaboration, Cardoso, J. V. d. M., Hedges, C., et al. 2018, Lightkurve: Kepler and TESS time series analysis in Python, Astrophysics Source Code Library, record ascl:1812.013 <http://ascl.net/1812.013>
- Lomb, N. R. 1976, *Ap&SS*, 39, 447, doi: [10.1007/BF00648343](https://doi.org/10.1007/BF00648343)
- Luna, G. J. M., & Sokoloski, J. L. 2007, *ApJ*, 671, 741, doi: [10.1086/522576](https://doi.org/10.1086/522576)
- Maehara, H. 2014, *Journal of Space Science Informatics Japan*, 3, 119
- Magdolen, J., Dobrotka, A., Orío, M., et al. 2023, *A&A*, 675, A140, doi: [10.1051/0004-6361/202345935](https://doi.org/10.1051/0004-6361/202345935)
- Merc, J. 2025, *Galaxies*, 13, 49, doi: [10.3390/galaxies13030049](https://doi.org/10.3390/galaxies13030049)
- Merc, J., Beck, P. G., Mathur, S., & García, R. A. 2024, *A&A*, 683, A84, doi: [10.1051/0004-6361/202348116](https://doi.org/10.1051/0004-6361/202348116)
- Merc, J., & Boffin, H. M. J. 2025, *A&A*, 695, A61, doi: [10.1051/0004-6361/202553789](https://doi.org/10.1051/0004-6361/202553789)
- Merc, J., Gális, R., Wolf, M., Leedjäv, L., & Teyssier, F. 2019, *Open European Journal on Variable Stars*, 197, 23, doi: [10.48550/arXiv.1905.04251](https://doi.org/10.48550/arXiv.1905.04251)
- Mikolajewska, J. 1996, in *Astrophysics and Space Science Library*, Vol. 208, *IAU Colloquium 158: Cataclysmic Variables and Related Objects*, ed. A. Evans & J. H. Wood, 335, doi: [10.1007/978-94-009-0325-8_102](https://doi.org/10.1007/978-94-009-0325-8_102)
- Mikolajewska, J., Kenyon, S. J., Mikolajewski, M., Garcia, M. R., & Polidan, R. S. 1995, *AJ*, 109, 1289, doi: [10.1086/117361](https://doi.org/10.1086/117361)
- Mikolajewska, J., Kolotilov, E. A., Shenavrin, V. I., & Yudin, B. F. 2002, in *Astronomical Society of the Pacific Conference Series*, Vol. 261, *The Physics of Cataclysmic Variables and Related Objects*, ed. B. T. Gänsicke, K. Beuermann, & K. Reinsch, 645
- Mikolajewska, J., Kolotilov, E. A., Shugarov, S. Y., Tatarnikova, A. A., & Yudin, B. F. 2003, in *Astronomical Society of the Pacific Conference Series*, Vol. 303, *Symbiotic Stars Probing Stellar Evolution*, ed. R. L. M. Corradi, J. Mikolajewska, & T. J. Mahoney, 151. <https://arxiv.org/abs/astro-ph/0210492>
- Munari, U. 2019, arXiv e-prints, arXiv:1909.01389, doi: [10.48550/arXiv.1909.01389](https://doi.org/10.48550/arXiv.1909.01389)
- Mürset, U., Nussbaumer, H., Schmid, H. M., & Vogel, M. 1991, *A&A*, 248, 458
- Ricker, G. R., Winn, J. N., Vanderspek, R., et al. 2014, in *Society of Photo-Optical Instrumentation Engineers (SPIE) Conference Series*, Vol. 9143, *Space Telescopes and Instrumentation 2014: Optical, Infrared, and Millimeter Wave*, ed. J. Oschmann, Jacobus M., M. Clampin, G. G. Fazio, & H. A. MacEwen, 914320, doi: [10.1117/12.2063489](https://doi.org/10.1117/12.2063489)
- Scargle, J. D. 1982, *ApJ*, 263, 835, doi: [10.1086/160554](https://doi.org/10.1086/160554)
- Sekeráš, M., Skopal, A., Shugarov, S., et al. 2019, *Contributions of the Astronomical Observatory Skalnaté Pleso*, 49, 19. <https://arxiv.org/abs/1904.05555>
- Shappee, B. J., Prieto, J. L., Grupe, D., et al. 2014, *ApJ*, 788, 48, doi: [10.1088/0004-637X/788/1/48](https://doi.org/10.1088/0004-637X/788/1/48)
- Skopal, A. 1998, *A&A*, 338, 599
- Skopal, A. 2003, *A&A*, 401, L17, doi: [10.1051/0004-6361:20030332](https://doi.org/10.1051/0004-6361:20030332)
- Skopal, A. 2005, *A&A*, 440, 995, doi: [10.1051/0004-6361:20034262](https://doi.org/10.1051/0004-6361:20034262)
- Skopal, A., Shugarov, S., Vaňko, M., et al. 2012, *Astronomische Nachrichten*, 333, 242, doi: [10.1002/asna.201111655](https://doi.org/10.1002/asna.201111655)
- Skopal, A., Tarasova, T. N., Wolf, M., Dubovský, P. A., & Kudzej, I. 2018, *ApJ*, 858, 120, doi: [10.3847/1538-4357/aabc11](https://doi.org/10.3847/1538-4357/aabc11)
- Skopal, A., Teodorani, M., Errico, L., et al. 2001, *A&A*, 367, 199, doi: [10.1051/0004-6361:20000413](https://doi.org/10.1051/0004-6361:20000413)
- Skopal, A., Tarasova, T. N., Cariková, Z., et al. 2011, *A&A*, 536, A27, doi: [10.1051/0004-6361/201116969](https://doi.org/10.1051/0004-6361/201116969)
- Skopal, A., Shugarov, S. Y., Sekeráš, M., et al. 2017, *A&A*, 604, A48, doi: [10.1051/0004-6361/201629593](https://doi.org/10.1051/0004-6361/201629593)
- Skopal, A., Shugarov, S. Y., Munari, U., et al. 2020, *A&A*, 636, A77, doi: [10.1051/0004-6361/201937199](https://doi.org/10.1051/0004-6361/201937199)
- Sokoloski, J. L., & Bildsten, L. 1999, *ApJ*, 517, 919, doi: [10.1086/307234](https://doi.org/10.1086/307234)
- Sokoloski, J. L., Luna, G. J. M., Mukai, K., & Kenyon, S. J. 2006a, *Nature*, 442, 276, doi: [10.1038/nature04893](https://doi.org/10.1038/nature04893)
- Sokoloski, J. L., Kenyon, S. J., Espey, B. R., et al. 2006b, *ApJ*, 636, 1002, doi: [10.1086/498206](https://doi.org/10.1086/498206)
- VanderPlas, J. T. 2018, *ApJS*, 236, 16, doi: [10.3847/1538-4365/aab766](https://doi.org/10.3847/1538-4365/aab766)
- Zechmeister, M., & Kürster, M. 2009, *A&A*, 496, 577, doi: [10.1051/0004-6361:200811296](https://doi.org/10.1051/0004-6361:200811296)